UNIVERSITY OF LEEDS

This is a repository copy of *Rapid solidification of AlCoCrFeNi2.1 High-entropy Alloy*.

White Rose Research Online URL for this paper:
https://eprints.whiterose.ac.uk/182923/

Version: Accepted Version

Article:
Nassar, A, Mullis, A orcid.org/0000-0002-5215-9959, Cochrane, R et al. (3 more authors) (2022) Rapid solidification of AlCoCrFeNi2.1 High-entropy Alloy. Journal of Alloys and Compounds, 900. 163350. ISSN 0925-8388

https://doi.org/10.1016/j.jallcom.2021.163350

© 2022, Elsevier. This manuscript version is made available under the CC-BY-NC-ND 4.0 license http://creativecommons.org/licenses/by-nc-nd/4.0/.

Reuse
This article is distributed under the terms of the Creative Commons Attribution-NonCommercial-NoDerivs (CC BY-NC-ND) licence. This licence only allows you to download this work and share it with others as long as you credit the authors, but you can't change the article in any way or use it commercially. More information and the full terms of the licence here: https://creativecommons.org/licenses/

Takedown
If you consider content in White Rose Research Online to be in breach of UK law, please notify us by emailing eprints@whiterose.ac.uk including the URL of the record and the reason for the withdrawal request.

White Rose university consortium
Universities of Leeds, Sheffield & York

eprints@whiterose.ac.uk
https://eprints.whiterose.ac.uk/

Rapid Solidification of $AlCoCrFeNi_{2.1}$ High-Entropy Alloy

A. Nassar[*], A. Mullis[*], R. Cochrane[*], Z. Aslam[*], S. Micklethwaite[*], L. Cao[**]

[*]*School of Chemical & Process Engineering, University of Leeds, Leeds, LS2 9JT, UK*

[**]*Department of Materials Science and Engineering, North China University of Technology, Beijing 100144, China*

Abstract

In this work the effect of cooling rate on the dual-phase ($L1_2$/B2) $AlCoCrFeNi_{2.1}$ Eutectic High-Entropy Alloy was investigated. $AlCoCrFeNi_{2.1}$ powders were made using a drop-tube facility, achieving powders of sizes ranging from 850 µm ≤ d < 1000 µm to 38 µm ≤ d < 53 µm with corresponding estimated cooling rates of 114 Ks^{-1} to 1.75×10^6 Ks^{-1} respectively. Average interlamellar spacing decreases from 2.10 µm in the as-cast alloy to 348 nm in the powders of the 38 µm < d < 53 µm size fraction. Although decreased interlamellar spacing is expected to enhance microhardness, such a relation was not as strong as expected, with microhardness of the powders found to vary only slightly from an average value of 340 $Hv_{0.03}$. This unexpected result is explained via the observation of increased FCC volume fraction. With increasing cooling rate, the microstructure of $AlCoCrFeNi_{2.1}$ was found to evolve gradually from regular eutectic to colony eutectic, followed by dendritic with eutectic the interdendritic regions. In particles of size d < 212 µm BCC dendrites were observed, either dominating the structure or coexisting with FCC dendrites.

Keywords: Eutectic High-Entropy Alloy; Interlamellar spacing; Cooling rate; Microhardness; Disorder Trapping.

1. Introduction

Comprising at least five elements in near equimolar ratios, High-Entropy Alloys (HEAs) offer an uncharted area of alloy discovery due to their vast composition space. Contrary to the pre-2005 belief held by the metallurgical community that the concept of multi-principal elements leads to complex and mostly brittle phases, many HEAs have shown simple crystal-structures such as FCC, BCC, FCC+BCC or HCP [1,2]. These simple structures arise due to the high configurational entropy of HEAs which stems from the large number of components which they contain. This high entropy leads to their simple solid solutions having reduced Gibbs free energy, thus allowing their formation [3].

Although HEAs have drawn large academic interest in recent years due to their outstanding mechanical and thermal properties [4], many recent investigations have been taking the route of developing Eutectic High-Entropy Alloys (EHEAs) [5–7], with the aim of creating a strength vs ductility balance [8]. $AlCoCrFeNi_{2.1}$ is a EHEA which has drawn significant interest in the past few years due to its lamellar structure of alternating FCC and BCC phases, giving it a rare strength-ductility balance due to the soft FCC phase and hard BCC phase [9]. First reported in 2014 [9], $AlCoCrFeNi_{2.1}$ attracted immediate attention, making it one of the most investigated EHEAs today. Several early studies investigated the mechanical properties of $AlCoCrFeNi_{2.1}$, determining values for the yield strength, elongation to failure and fracture stress of 620 MPa, 17% and 944 MPa, respectively [5,9]. Volume fractions of the $L1_2$ and B2 phases of as-cast $AlCoCrFeNi_{2.1}$ were found to be around 65 % and 35 % respectively [5,8].

As with most HEAs, rapid solidification of $AlCoCrFeNi_{2.1}$ has been investigated only to a brief extent. In 2017 $AlCoCrFeNi_{2.1}$ powders were produced by gas atomization [10] and $AlCoCrFeNi_{2.1}$ ribbons were produced via melt-spinning [11]. The powders produced from the gas atomization study were typically 20-80 μm in diameter, with larger particles being remelted. Although not quantified by the authors, the cooling rates in that study are likely to overlap with those for the powders produced here. In this respect, we note that cooling rates during gas atomization tend to be somewhat lower than in drop-tube processing for similar sized particles, this being due to the higher thermal load represented by the metal in gas atomization [12]. In this work, we report a much wider range of powder sizes and consequently a larger variety of cooling rates and, in turn, microstructures. As such, the larger powders produced in our work undergo cooling rates that are lower than those typically achieved by gas atomisation, whereas our smaller powders undergo cooling rates relatable to those of selective laser melting (SLM). Cooling rates observed in SLM can reach the order of 10^6 [13], meaning that the cooling rates achieved in our work can be useful in guiding SLM of the $AlCoCrFeNi_{2.1}$ alloy. Generally, the wide range of cooling rates we present overlaps with those of various manufacturing processes and as such, gives a detailed insight to controlling the microstructure of $AlCoCrFeNi_{2.1}$ and correlating the microhardness of the alloy with cooling rate.

Although a recent machine-learning-based work has significantly simplified HEA discovery [14], the search for EHEAs has mainly been directed by a search for elements which form binary eutectic compositions with all, or most, of the elements in a chosen promising system [15,16]. $CoCrFeNiX_y$, where X is one of Nb, Zr, Hf and Ta, is one such example, with y being the average atomic fraction of element X at eutectic composition in each of the binaries [17]. Although this technique has shown success in unveiling several EHEAs, no studies have mentioned its use in deducing the $AlCoCrFeNi_{2.1}$ composition. However, given that AlNiCr is a well-known eutectic [18,19], Co and Fe may have simply been added to this base to form an HEA. Reaching the EHEA composition may have then been achieved by iteration, aided by intuition regarding the AlNiCr system.

Although exploring the composition space of HEAs is vital in advancing their development, relating HEA development to industrial relevance is equally important and currently lacking due to the field's relatively young age. EHEAs do well in bridging the gap between academic research and industrial practice in that they are suitable for practical large-scale casting (unlike most non-eutectic HEAs) [20,21]. Bridging this gap can also be achieved by exploring the effect of rapid solidification on the microstructures and properties of HEAs. With sluggish diffusion being a main characteristic in HEAs [22,23], the rate of coarsening at

elevated temperatures is minimal, leading to excellent retention of fine microstructures [6]. As such, the investigation of a Hall-Petch relationship in (E)HEAs is of great importance as rapid solidification may push the boundaries of their already outstanding mechanical properties.

Rapid solidification of $AlCoCrFeNi_{2.1}$ creates an opportunity of investigating the evolution of this EHEA's microstructure and mechanical properties with cooling rate. Considering the abundance of studies on as-cast HEAs, the rapid-solidification of HEAs is a topic in stark need of more investigation. Melt-spun $AlCoCrFeNi_{2.1}$ was shown to lose its lamellar structure and form precipitates on the grain boundaries [11]. However, cooling rates for this finding were not stated, making it difficult to draw connections between cooling rate and microstructural evolution. Similarly, cooling rates were not reported for the gas atomized particles produced by Ding *et al*. [10], although based upon other studies of gas atomization, we may conjecture these were of the order 10^4-10^5 K s^{-1}. In their powders, Ding *et al*. observed a blocky dendritic structure of FCC dendrites with an FCC/BCC interdendritic eutectic. Centrifugally cast $AlCoCrFeNi_{2.1}$, cooled at 450 K s^{-1}, showed an almost identical structure of FCC dendrites with an eutectic interdendritic region [24], albeit that the dendrites were somewhat better developed than those in the gas atomization study.

The work presented here investigates the effect of rapid solidification on the microstructure and microhardness of the $AlCoCrFeNi_{2.1}$ EHEA and $AlCoCrFeNi_{2.1}$ powders, with cooling rates ranging from 114 K s^{-1} to 1.75×10^6 K s^{-1} being obtained using a drop-tube facility. The range of cooling rates achieved in this study, as well as their magnitude, make this work extremely relevant as rapid cooling of the $AlCoCrFeNi_{2.1}$ and HEAs in general is in need of more investigation.

2. Experimental Details

2.1 Alloy preparation

An ingot of the $AlCoCrFeNi_{2.1}$ master alloy was prepared using an electric arc-furnace with a water-cooled copper hearth and a heating current of 230 A. The associated vacuum chamber was evacuated and purged with Argon four times before melting. To ensure homogeneity, the alloy was turned over and melted four times. Each of the constituent elements had a purity of > 99.9wt%. To form powders from the $AlCoCrFeNi_{2.1}$ master alloy, a drop-tube facility was used.

2.2 Drop tube experiment

A drop tube of 6.5m in length (schematic shown in Figure 1) was pre-evacuated to pressures below 10^{-4} Pa before being back-filled with 50 kPa of pure N_2 gas.

A 7g ingot of as-cast $AlCoCrFeNi_{2.1}$ was placed in an alumina crucible containing three holes at its base, and inductively heated using a 3 kW RF power supply until its melting point of around 1350 °C was attained. The melt was then ejected from the crucible using a differential pressure of 350 kPa. In most cases the droplets solidified containerlessly in-flight and were collected at the bottom of the drop-tube. The resulting powders were sieved into 10 standard diameter ranges: > 850 µm, 850–500 µm, 500–300 µm, 300–212 µm, 212–150 µm, 150–106 µm, 106–75 µm, 75–53 µm, 53–38 µm and < 38 µm.

To calculate the cooling rate of each powder size fraction, a heat balance for a droplet in free fall was used, considering heat transfer via convection, conduction and radiation from the droplet to its environment. This heat balance is expressed as [25]:

$$\frac{dT_d}{dt}[c_l(1-f)+c_s f]+L\frac{df}{dt}=\frac{6h}{\rho d}\left(T_d-T_g\right)+\frac{6\varepsilon\sigma_b}{\rho d}\left(T_d^4-T_g^4\right) \quad (1)$$

where T_g is the temperature of the gas used to back-fill the apparatus (N_2), c_s and c_l are the specific heat of the metal in the solid and liquid states, respectively, f is the solid fraction, ρ is the density of the solid metal, d the diameter of the droplet, ε the emissivity of the droplet surface, σ_b the Stefan–Boltzman constant, T_d is the instantaneous temperature of the particle and h is the heat transfer coefficient, which is evaluated according to the method outline in [25] assuming the particles attain terminal velocity within the tube during free fall.

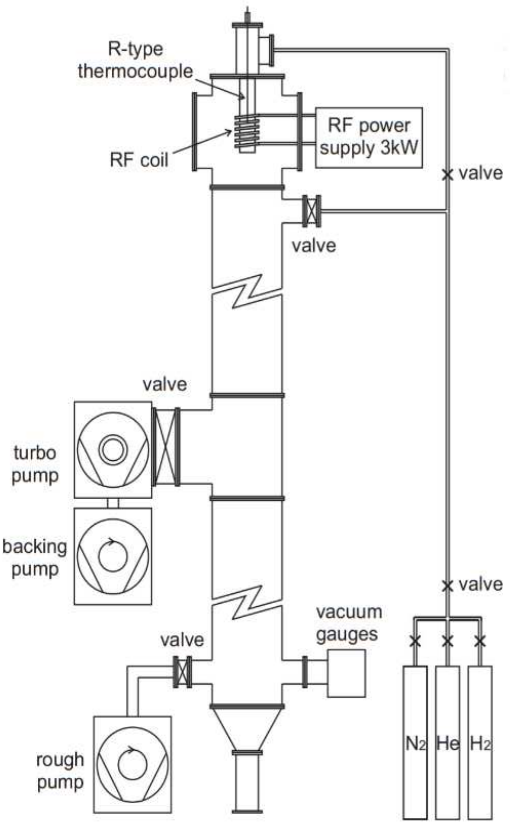

Figure 1. – Schematic of Drop-Tube apparatus used in this work [25].

The heat transfer coefficient, *h*, is given by:

$$h = \frac{\kappa_g}{d}(2.0 + 0.6\sqrt{Re}\,3\sqrt{Pr} \tag{2}$$

where κ_g is the thermal conductivity of the Nitrogen gas, Re is the Reynolds number and Pr is the Prandtl number. The Reynolds and Prandtl numbers are given by the following equations:

$$Re = \frac{v_g \rho_g D}{\eta_g} \quad (3)$$

$$Pr = \frac{c_g^p \eta_g}{\kappa_g} \quad (4)$$

Where v_g, ρ_g, η_g and c_g^p are the flow velocity, density and dynamic viscosity and specific heat of the back-fill gas, respectively. These properties of N_2 gas are presented in Table 1, together with the thermophysical properties of the $AlCoCrFeNi_{2.1}$ HEA. To calculate the properties of the $AlCoCrFeNi_{2.1}$ HEA estimates were made using properties of the constituent elements and their respective atomic ratios.

The drop tube processing of $AlCoCrFeNi_{2.1}$ allows powders to be achieved whose cooling history is more predictable than those achieved via an alternative method such as gas atomization. It has been highlighted previously that cooling rates reported by gas atomization studies vary considerably, such that discrepancies of such magnitude may not solely be attributed to differences in atomizing gas, pressure and particle size [12]. As such, for gas atomization, cooling rates obtained using a heat balance equation (such as shown in Equation 1) would not necessarily be expected to show strong agreement with cooling rates calculated by measurements of secondary dendrite arm spacing (SDAS). In contrast, drop tube studies have shown strong agreement between cooling rates inferred from SDAS measurements and those obtained via Equation 1 – one such agreement was recently shown in drop tube processed Al-2.85 wt% Fe [26].

Table 1

Properties of $AlCoCrFeNi_{2.1}$ HEA [27,28]					
c_s J kg^{-1} K^{-1}	c_l J kg^{-1} K^{-1}	ρ kg m^{-3}	L kJ kg^{-1}	ε	T_m K
525	544	7411	316	0.2	1593
Properties of N_2 Gas [29]					
T_g K	η_g	ρ kg m^{-3}	c_g^p J kg-1 K	κ_g	-
295	1.78×10^{-5}	1.16	1039	2.60×10^{-2}	

2.3 Sample analysis

The powders retrieved from the drop-tube were hot mounted using phenolic resin and ground using abrasive SiC paper down to size P2500. The samples were polished manually using diamond paste from 6 µm down to 1 µm - polishing was then continued automatically using colloidal silica. All samples were etched with *aqua regia* for 15 seconds to be observed under a scanning electron microscope (Hitachi SU8230). The SEM was used in backscattered electron detection mode to examine the microstructures of the samples and to obtain eutectic interlamellar spacing values. EDX analysis was used to analyse the composition of the phases observed in the microstructures.

XRD (Bruker D8) using Cu-Kα radiation and a 2θ scan rate of 1º/min with a range from 30º to 95º was used for phase identification. Microhardness measurements were performed (using Tukon 1202 Wilson hardness tester) on all powder sizes using a load of 300 gf with a dwell time of 10 seconds. Ten measurements were taken for each powder size to minimise standard error.

To measure the volume fraction of the phases present in the samples, ImageJ software was used. A selection was made of the region where the volume fraction is to be investigated. This was done in order to eliminate the dark background arising from the mounted compound which would otherwise distort the image intensity histogram. A threshold value for the micrograph in question was then adjusted to an appropriate value to achieve clear separation between the phases, which generally appear with a well-defined light/dark contrast in backscatter imaging. The particle was then analysed and 10 measurements were taken from different areas to calculate mean and standard error.

3. Results and discussion

Figure 2a shows the microstructure of as-cast $AlCoCrFeNi_{2.1}$ observed using backscatter SEM imaging. It is evident from Figure 2 that the as-cast microstructure shows a eutectic structure comprising a dark, Al and Ni rich phase and a light phase that is particularly rich in Cr (see line scan in Figure 2b). TEM analysis shown in Figure 3 was also carried out to reveal the crystallographic information of the constituent phase, the reflection spots of ordering crystal structures (highlighted by red circles), confirming that the dark and light phases (Figure 2) are ordered BCC (B2) and FCC ($L1_2$) phases. This is consistent with multiple results reported elsewhere [5,8,30,31]. As Cr is BCC (and a strong BCC stabilizer in Fe) it is rather unexpected that the Cr-rich phase forms an FCC structure. A study by Gao *et al*. has constructed the CoCrFeNi phase diagram, wherein, for the equimolar alloy, BCC is indeed the equilibrium phase at room temperature [32]. However, two different FCC phases (of different compositions) do occupy large parts of the CoCrFeNi phase space at elevated temperature.

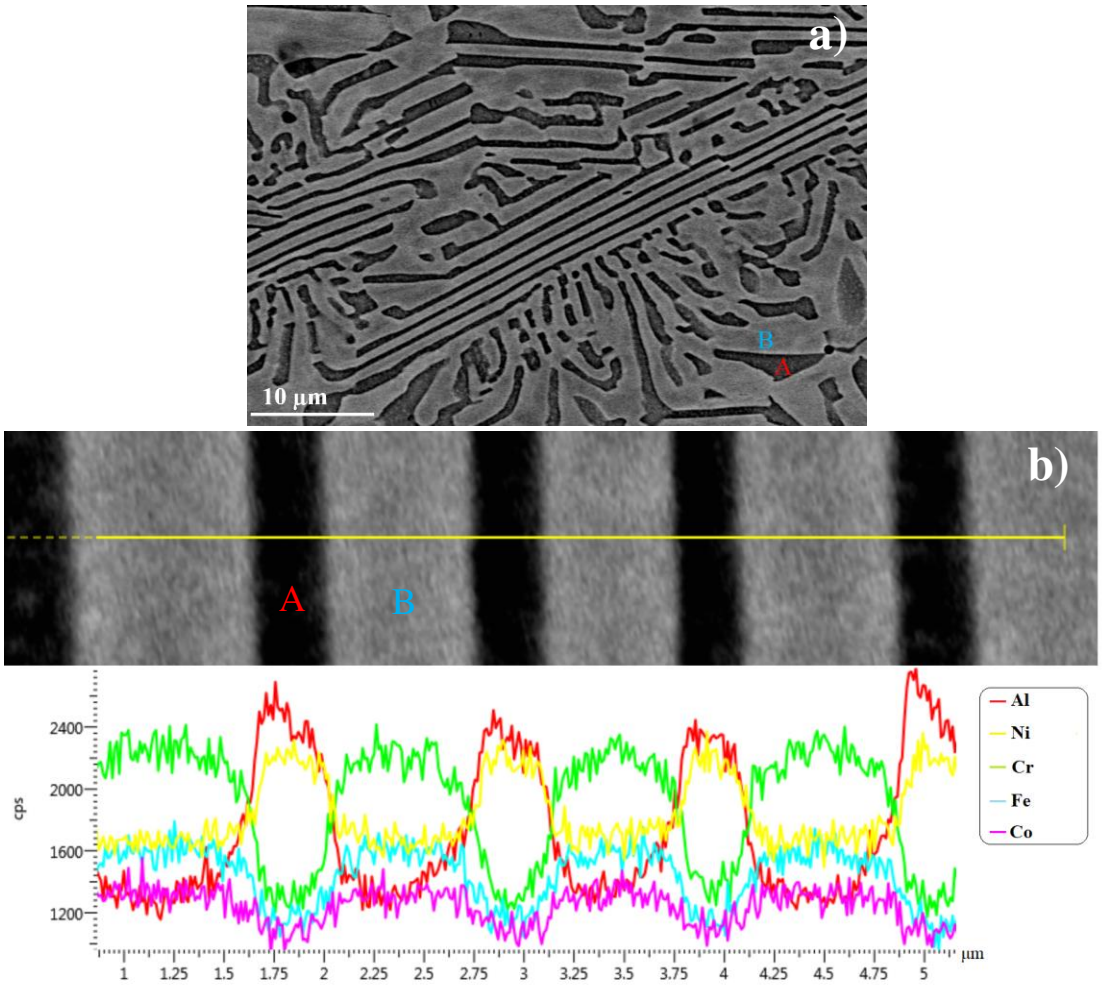

Figure 2: a) Microstructure of as-cast AlCoCrFeNi2.1 EHEA – Where A is the BCC phase and B is the FCC phase; **b)** Line-scan of as-cast $AlCoCrFeNi_{2.1}$ showing Al-Ni rich phase and Cr rich phase.

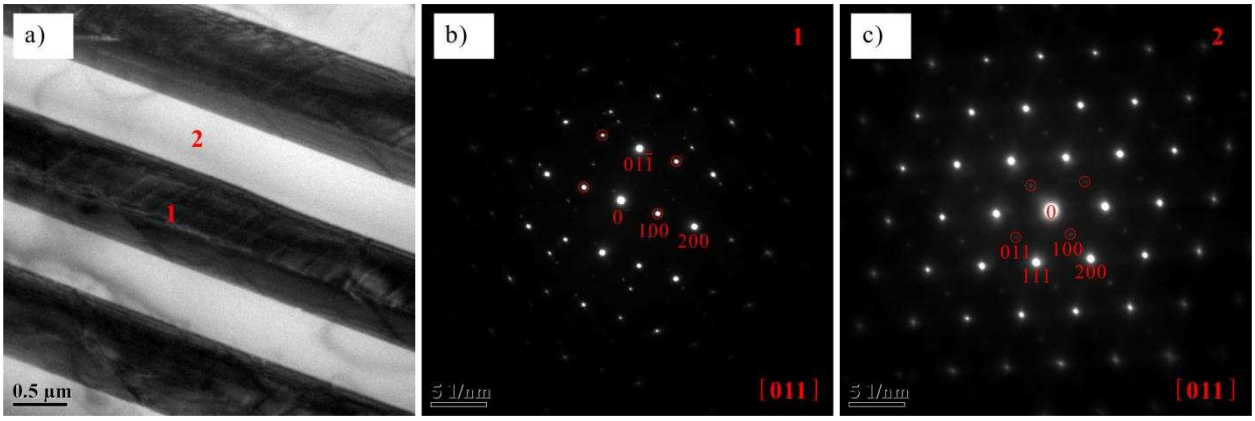

Figure 3: a) regular eutectic structure of the arc-melted AlCoCrFeNi2.1 alloy. **b)** and **c)** SAED patterns of the regions labeled 1 and 2, showing ordered B2 and ordered L12 structures, respectively.

The XRD pattern in Figure 4 confirms that an FCC/BCC duality is retained for all rapidly cooled powders, irrespective of cooling rate. However, it must be noted that due to the stochastic nature of nucleation, differences in microstructure exist between particles of the same size fraction albeit they experience similar cooling rates. Such differences are discussed in more detail below when we consider the droplet microstructure in detail. Figure 5 shows the relationship between droplet size and cooling rate, and serves as a good reference in correlating the microstructures presented throughout the body of this work to their respective cooling rates. The cooling rates presented in this work correspond to the lower bound of the aforementioned powder size fractions.

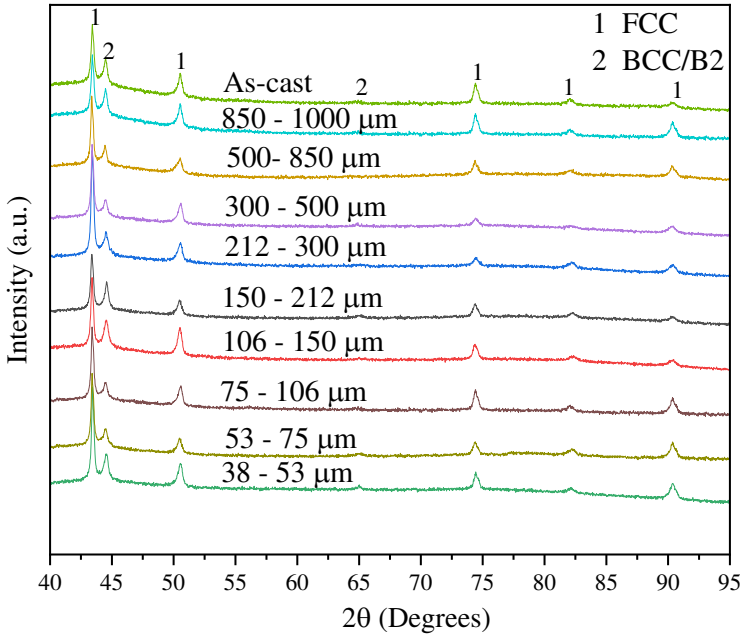

Figure 4: XRD patterns for $AlCoCrFeNi_{2.1}$ powders obtained via drop-tube processing.

Figure 6 illustrates the differences in the microstructure of $AlCoCrFeNi_{2.1}$ powders from various size fractions (hence various cooling rates). Figure 6a shows the well-documented regular eutectic with emanating facets, which has become characteristic of as-cast $AlCoCrFeNi_{2.1}$. Despite solidifying at an estimated cooling rate of 114 K s^{-1} (850 µm - 1000 µm) the microstructure in Figure 6a is not significantly different from the as-cast microstructure. Figure 6b shows that cellular eutectic growth becomes more prevalent in the 150 - 212 µm sieve-fraction. This is followed by a predominantly dendritic structure with a eutectic in the interdendritic region, shown in Figure 6c (53 - 75 µm). That is, with increasing cooling rate, and therefore increasing undercooling in the liquid prior to nucleation, the solidification of $AlCoCrFeNi_{2.1}$ transitions from the primary solidification constituent being eutectic to the primary solidification phase being FCC dendritic. A similar observation has been made by Zheng et. *al* [33], outlining a predominantly dendritic structure as withdrawal rate is increased during directional solidification of $AlCoCrFeNi_{2.1}$. In our work, dendrites first appear in the 212 - 300 µm size fraction and the transition from regular to colony eutectic is also observed at this cooling rate. All the constituents of this growth morphology are coincidentally present in one particle displayed in Figure 7.

We observe departure from eutectic growth at cooling rates around 10^4 K/s, indicating that sufficient undercooling is achieved at this cooling rate for the eutectic to dendritic transformation to occur. A study

on the rapid solidification of the AgCuGe (ternary eutectic alloy) achieves a similar cooling rate of 9.3 × 10^3 K/s, although it was shown in this alloy that the undercooling in this condition is not sufficient for departure from eutectic growth [34]. Unlike the $AlCoCrFeNi_{2.1}$ alloy, an anomalous eutectic is observed in AgCuGe at intermediate cooling rates prior to dendritic growth. A rapid solidification study by Rios et al. [35] on AlNbNi observes a transition from a regular eutectic to a colony eutectic very similar to the one we observe in Figure 6b. Rios et al. make no observation of dendritic growth, although this is likely to be due to a relatively low cooling rate (1000 K/s), which in turn does not achieve the required undercooling for the eutectic to dendritic transformation. In systems regularly selected for undercooling studies, such as the Ag-

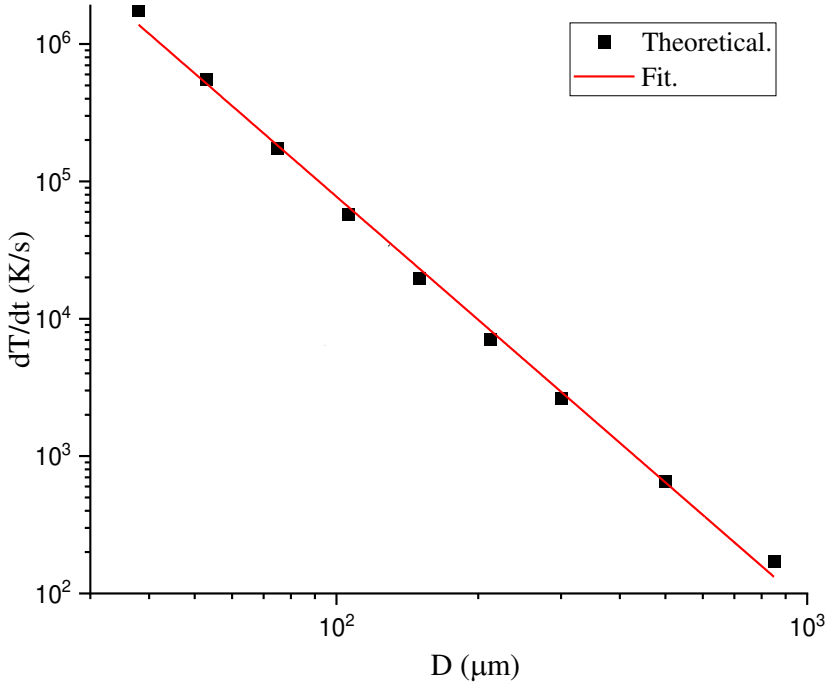

Figure 5: Estimated cooling rates of $AlCoCrFeNi_{2.1}$ powders as a function of powder diameter.

Cu alloy, an undercooling as small as 70 K is sufficient to observe dendritic growth [36]. As studies on rapid solidification of EHEAs are rather uncommon, our study is one which strongly invites further research to investigate the range of undercoolings required for dendritic growth in EHEAs. As we have also shown that an anomalous eutectic is not observed in $AlCoCrFeNi_{2.1}$ in any given sieve fraction, it is worth exploring in more detail the microstructure development of EHEAs during their departure from regular eutectic growth.

Finally, at the highest cooling rates (smallest droplets), it is possible to observe particles with a dendritic microstructure and no eutectic in the interdendritic region – shown in Figure 6d. This indicates that, in some instances, the residual undercooling following recalescence is sufficient to inhibit eutectic formation. It must be noted that due to the stochastic nature of nucleation, not all particles in the 38 - 53 μm size-fraction experience this critical undercooling and many particles retain the eutectic structure in the interdendritic region (see Figure 8). In Figure 6 it can also be visually observed that the primary FCC volume fraction increases with cooling rate. Figure 9 confirms and quantifies this observation, showing the increase in volume fraction of the primary (dendritic) FCC phase with increasing cooling rate. It was found that the total FCC volume fraction in the largest powders is 63.7 %. Due to the relatively low cooling rate of these powders, this is expectedly similar to the FCC fraction in the as-cast alloy (65.3 %) and in both cases is in accord with the FCC volume fraction reported in the literature. With increasing cooling rate, we observed

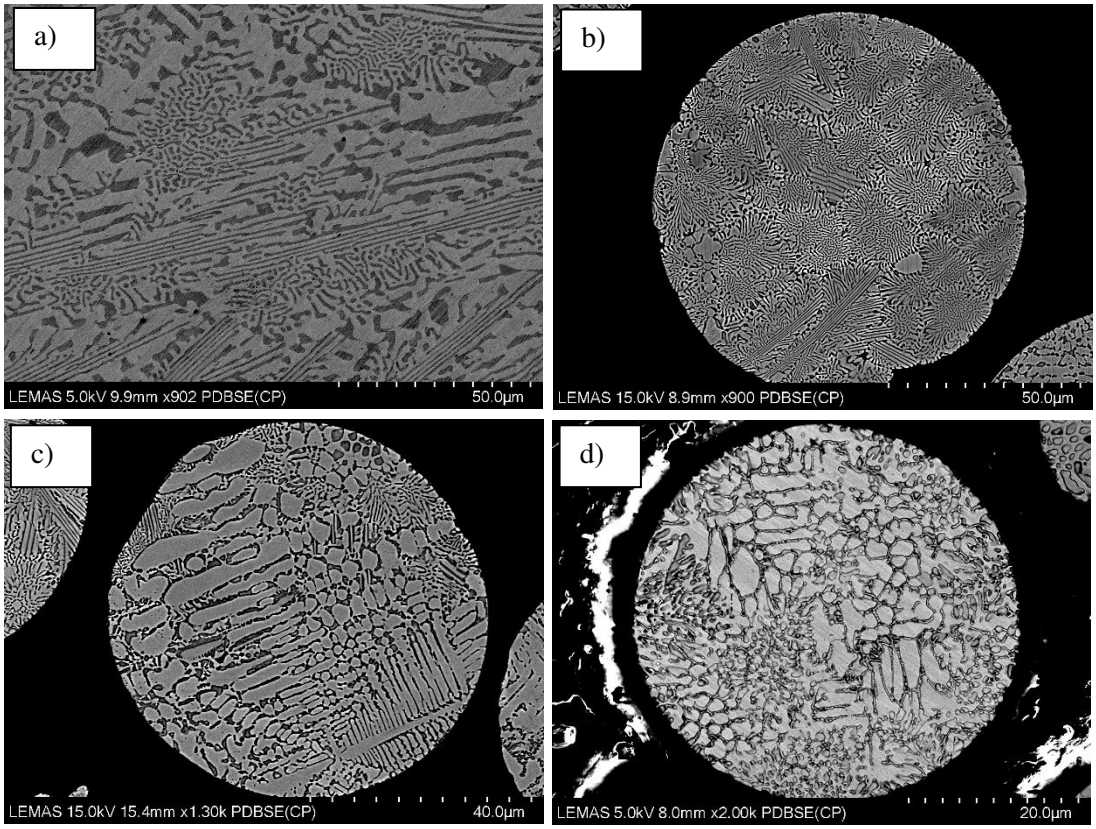

Figure 6: Microhardness morphology as powder size decreases, showing increasing volume fraction of FCC phase. Powders from a) to d) are taken from powder size fractions 850 – 1000 µm, 150 – 212 µm, 53 – 75 µm and 38 – 53 µm, respectively.

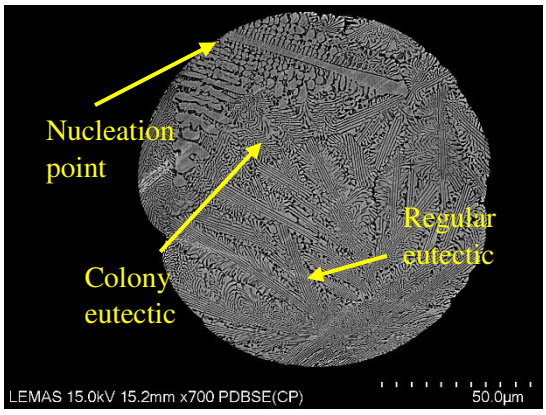

Figure 7: Particle from 75 – 106 µm size fraction with clear nucleation point leading to dendritic region. Colony and regular eutectic regions are also visible.

that the primary FCC volume fraction increases monotonically, reaching an average maximum of 85% in powders of the 38 - 53 µm size-fraction. The total FCC volume fraction was found to reach a maximum of 88%. It is also evident from Figure 6 that the volume fraction of the eutectic phase decreases, and this can also be inferred quantitatively from Figure 9. With increasing cooling rate, the microstructures expectedly become finer, leading to decreased lamellar spacings. As expected, interlamellar spacing is refined with higher cooling rates, ranging from 1.63µm to 0.35µm in the largest and smallest powder-size fractions, respectively. Considering that average interlamellar spacing in the as-cast microstructure was found to be

2.1 µm, it is clear that interlamellar spacing is refined significantly as cooling rate increases. Figure 10 shows the relation between interlamellar spacing and cooling rate on a logarithmic scale.

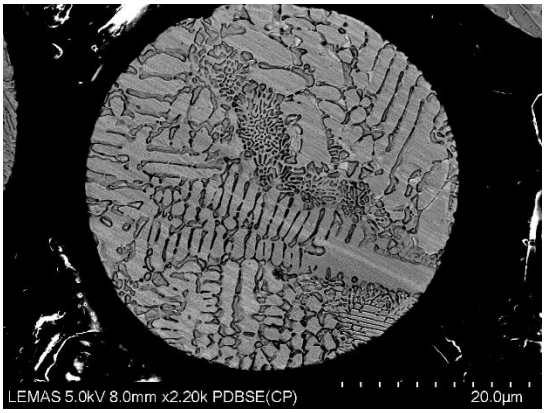

Figure 8: Particle from 38 – 53 µm size fraction with eutectic microstructure retained in the interdendritic region.

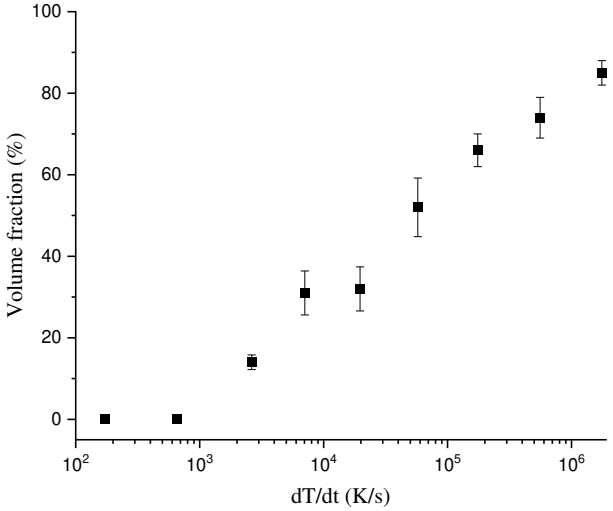

Figure 9: Increasing dendritic volume fraction with increasing cooling rate.

By analysing the $AlCoCrFeNi_{2.1}$ powders using TEM, it is observed that the rapid cooling achieved via drop-tube processing is sufficient to inhibit $L1_2$ ordering at relatively low cooling rates. This is shown by the TEM analysis in Figure 11, where the SAD patterns of a particle from the 500 - 850 µm size fraction are presented. Figure 11a presents the regions from which the SAD patterns are taken, whereby the pattern in Figure 11a shows that B2 ordering is retained (see superlattice spots) and Figure 11b shows that $L1_2$ ordering is lost. This observation is in accord with the argument of Ding et al. that the B2 – BCC (order-disorder) transformation requires larger cooling rates to be achieved than the $L1_2$ – FCC transformation. Ding et al. also argue that disorder trapping of the B2 phase is expected for $AlCoCrFeNi_{2.1}$ gas atomised powders 20 - 80 µm in size [10]. Although this argument is not supported by TEM analysis, Figure 11 confirms that the statement of Ding et al. is a reasonable one, as B2 ordering is retained for $AlCoCrFeNi_{2.1}$ particles of 500 - 850 µm. Further, Figure 11e shows that B2 ordering is lost in a particle from the 38 - 53

µm size fraction. As expected, $L1_2$ ordering is of course inhibited in this particle as well (see Figure 11f), as it experiences a larger cooling rate than the 500 - 850 µm particle. As such, we can concluded that a cooling rate of 650 K s^{-1} can lead to disorder trapping of the $L1_2$ phase but a higher cooling rate is required for disorder trapping of the B2 phase. Although further TEM analysis would be required to reveal a closer

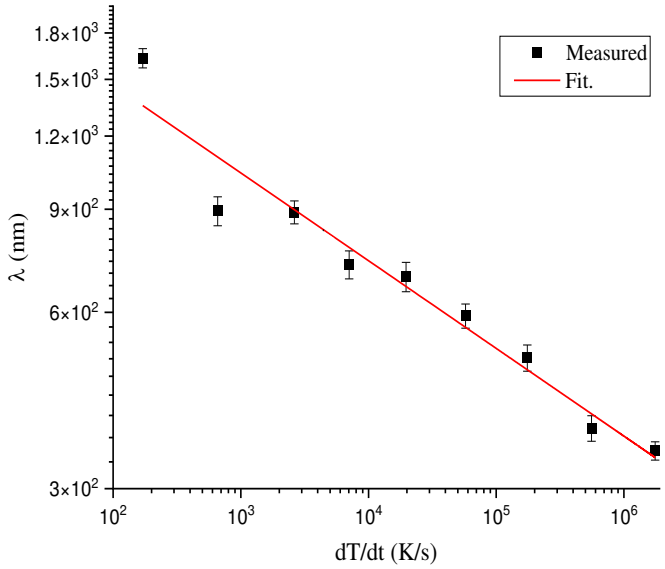

Figure 10: Interlamellar spacing versus cooling rate for $AlCoCrFeNi_{2.1}$ powders.

estimate of the exact cooling rate required for the B2 – BCC transformation, here we confirm that a cooling rate of 1.75×10^6 K s^{-1} is enough.

A morphology unobserved previously in $AlCoCrFeNi_{2.1}$ is worth noting and appears in particles of size $d <$ 212 µm (shown in Figure 12a), where a dark dendritic phase appears to have nucleated as the primary phase. From this dark dendritic phase, a lighter dendrite has nucleated and is observed growing around its perimeter. Although the light, Cr-rich, dendrites have previously been observed in rapidly cooled $AlCoCrFeNi_{2.1}$ [10][24], this is, as far as we are aware, the first instance of dendrites of the darker BCC phase being observed in dendritic form.

Figure 12b shows that this dark, Al-Ni rich phase can grow to dominate the microstructure, with the light phase forming the interdendritic region. Therefore, we note that some particles are observed to only have FCC dendrites (see any of Figures 7 and 8) and others to have only BCC dendrites. The EDX scan in Figure 13 shows that the dark dendrites are the Al-Ni rich, BCC phase, whereas Figure 14 shows a lighter-contrast dendrite depleted in aluminium and nickel in the microstructure of a particle from the 53 - 75µm size fraction. To explain the structures in Figure 12, the undercooling of the particles must be considered as follows. At most undercoolings the BCC phase will grow as its B2 variant, which will give the disordered FCC phase a growth advantage, it being known that disordered phases grow significantly faster than ordered phases [37]. However, if the undercooling is sufficient for disorder trapping in the BCC phase (i.e. a B2 to BCC transition) the growth advantage of the FCC phase will be much reduced, wherein a suitable heterogenous nucleant may favour the growth of BCC dendrites over FCC. Moreover, if recalescence leads to a reduction in undercooling during growth, a transition back to B2 growth would significantly reduce the BCC growth rate, leading to overgrowth of the BCC phase by FCC dendrites, as appears to be the case in Figure 12a and Figure 13.

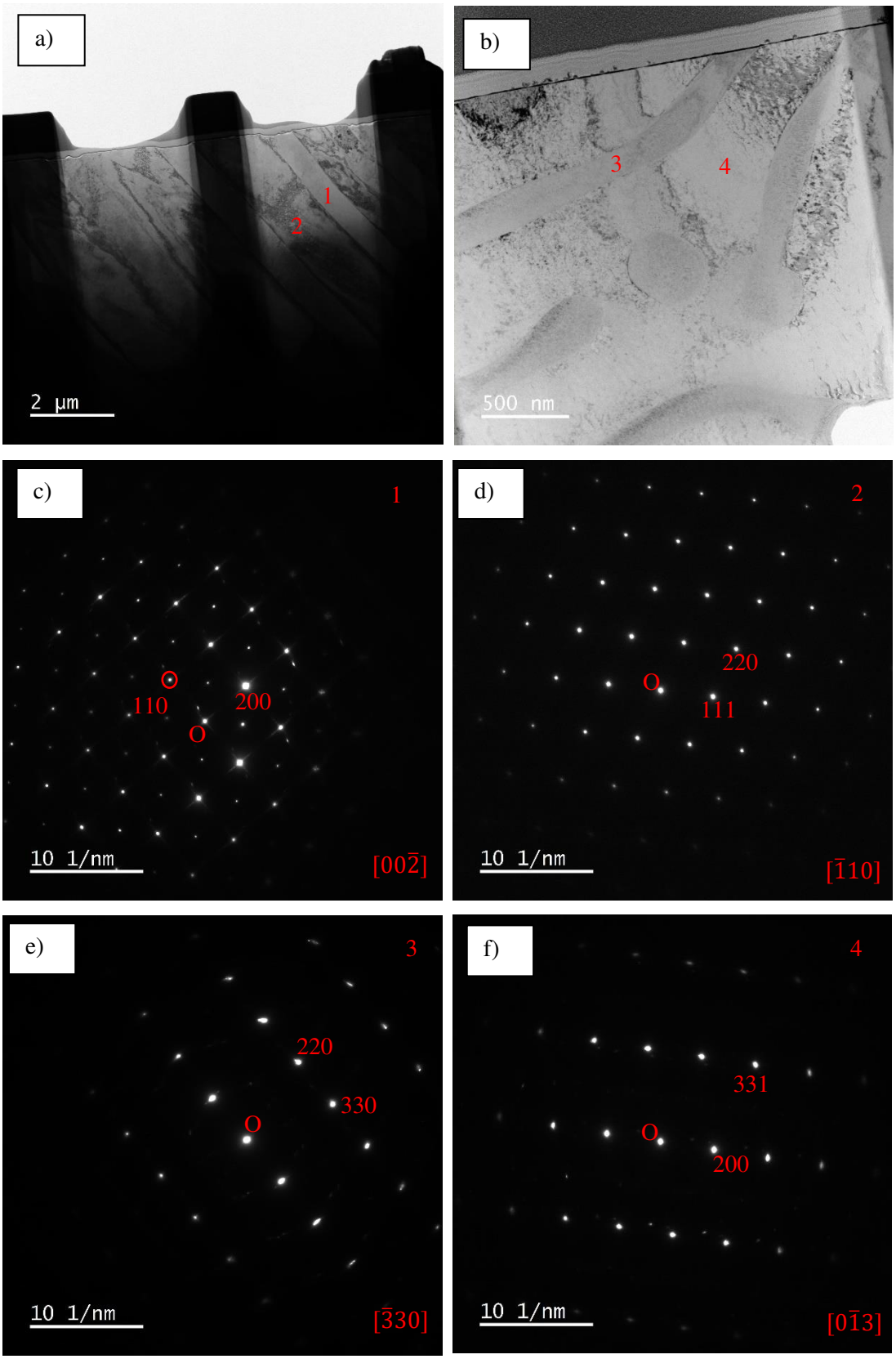

Figure 11: a) Lamellar region from 500 - 850µm size particle, with corresponding SAED patterns showing ordered B2 and disordered FCC structures in regions labelled 1 and 2, respectively. **b)** Irregular lamellae from 38 – 53 µm size particle, with corresponding SAED patterns showing disordered BCC and disordered FCC structures in regions labelled as 3 and 4, respectively.

Considering the structure seen in Figure 12b where only BCC dendrites are observed, this is a case where sufficient undercooling has allowed the BCC phase to dominate the microstructure before the occurrence of the BCC to B2 transformation. This also provides an explanation for the absence of BCC dendrites in larger sieve fractions, where undercooling is insufficient to facilitate disorder trapping in the B2 phase [38]. As B2 disorder trapping requires larger cooling rates relative to the $L1_2$ – FCC transformation [39], it comes as no surprise that in larger powders FCC dendrites nucleate as the primary phase. Namely, any growth competition between a disordered FCC and an ordered B2 phases will heavily favour FCC growth, making growth of the BCC phase unlikely. Although we have unveiled that BCC dendritic growth occurs in powders $d < 212$ µm in size, measuring the undercooling required for this growth condition is not possible during drop-tube experiments. However, it has previously been estimated that the undercooling of Co-Cu droplets of similar size, based on the kinetics of monotectic liquid phase separation, is 210-250 K [40]. This value is in-line with the undercooling observed to mediate the order-disorder transformation in other materials [40].

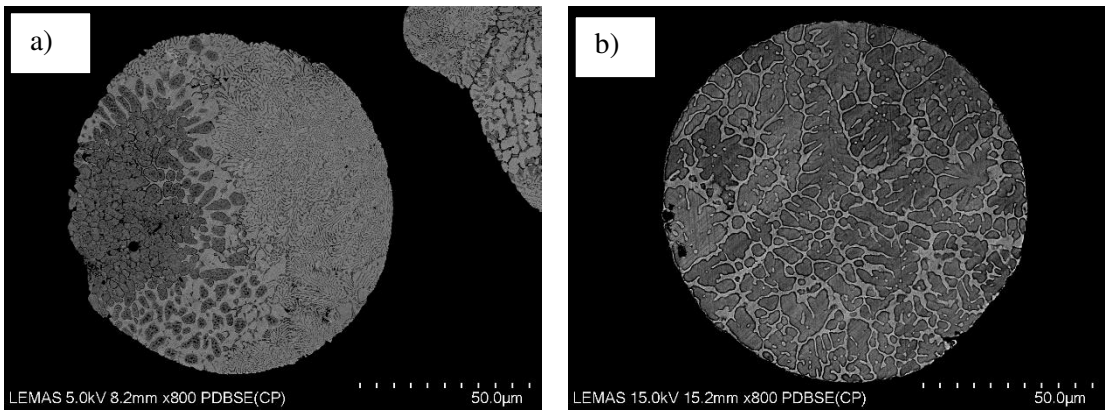

Figure 12 a) BCC dendrites observed within particles of 75 – 106 µm size fraction **b)** BCC dendrites extending beyond localized region and occupying full microstructure.

Considering the lamellar as-cast structure, smaller powders would be expected to have superior microhardness values as per the Hall-Petch relation i.e. $\sigma_y = \sigma_0 + \kappa_H \lambda^{-0.5}$; where σ_y is the yield strength of the material, σ_0 is the friction stress, κ_H is Hall-Petch coefficient and λ is the interlamellar spacing [6]. Although it is a weak relation, the Hall-Petch effect is observed in the $AlCoCrFeNi_{2.1}$ powders obtained via drop-tube processing, see Figure 15. The Hall-Petch relation may have been observed more strongly if the microhardness tests were intentionally conducted on lamellar regions of the powders. However, such microhardness values would be unrepresentative of $AlCoCrFeNi_{2.1}$ powders and are likely to create a distorted idea of the true overall microhardness of the powders. For those reasons, the microhardness values presented in this work are obtained with the indentations being made in randomly chosen locations of the droplets.

Despite the Hall-Petch correlation, the microhardness of $AlCoCrFeNi_{2.1}$ powders does not vary greatly from an average value of around 340 $Hv_{0.03}$, even though the lamella spacing varies by a factor of 4.5 over this range of particle sizes. We believe this weak Hall-Petch relation is explained by the dominance of the primary FCC phase in smaller droplets. As the FCC phase is the softer phase [9], its increased presence with increased cooling rate is expected to cancel out the strengthening due to scale refinement which would otherwise be observable. Meanwhile, it is worth drawing back on the inhibited atomic ordering due to the large cooling rates. As the disordered phases have more slip planes, we suggest that disorder-trapping may

also be a factor which hinders the alloy powders' hardness [6]. As both phenomena occur in conjunction, ambiguity arises in identifying which of them has a more detrimental effect on the microhardness of the powders. However, for the powders in the 850 - 1000 µm size-fraction, it is likely that disorder trapping is the main factor contributing to the lower-than-expected microhardness value. This is because the phase volume fractions in the droplets of this size do not differ significantly from the as-cast alloy. Yet, the average microhardness in this size fraction is 12 % smaller than that of the as-cast alloy. As such, this drop in microhardness could be attributed to the disorder trapping of the $L1_2$ phase.

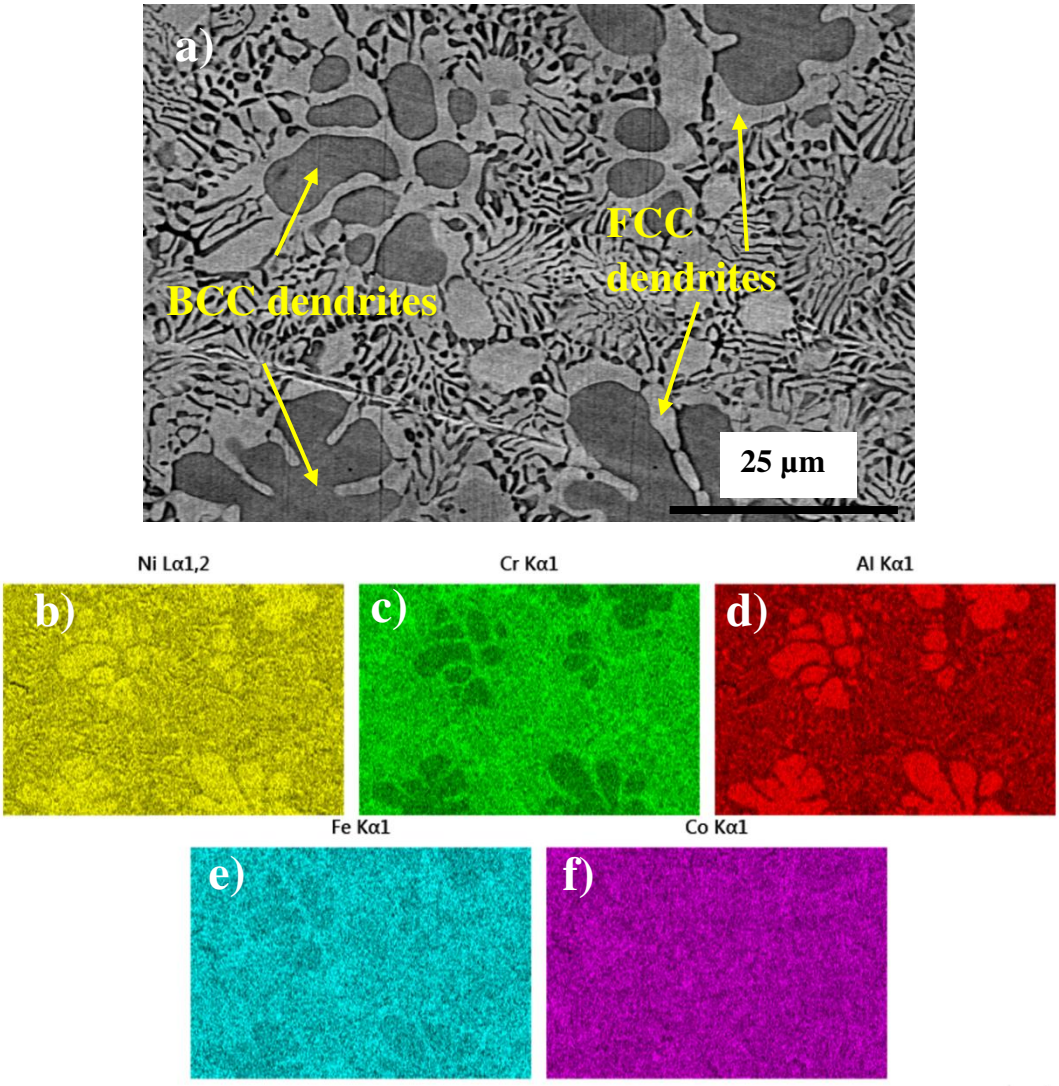

Figure 13: Al and Ni rich (BCC) dendrites of parasite-like phase observed within the 106 µm < *d* < 150 µm and 150 µm < *d* < 212 µm

Powders from the 150 - 212 µm size-fraction were chosen to be annealed for 30 minutes at 700 ºC, in order to investigate the effect on microhardness. The annealed powders showed an average microhardness that is 32 % higher than the non-annealed powders of the same size range (see Figure 15). However, the annealed powders are in fact expected to show reduced microhardness, as lamellar spacing increases by an average of 200 nm due to annealing. Figure 16 shows a micrograph of the annealed sample, where the slightly

coarsened λ values are displayed. As such, the increase in microhardness could be justified using the idea that the disordered phases in the powders may be metastable. If that is the case, annealing the powders is expected to supply the driving force required for the disorder to order transformations to take place, thus improving the microhardness due to the reduced number of slip planes in ordered phases. To conclude, the powders do show a Hall-Petch relationship (albeit a weak one) despite the impacts of disorder trapping and increased FCC volume fraction. This is consistent with the occurrence of grain refinement but with the mechanical benefits being countered by these two effects.

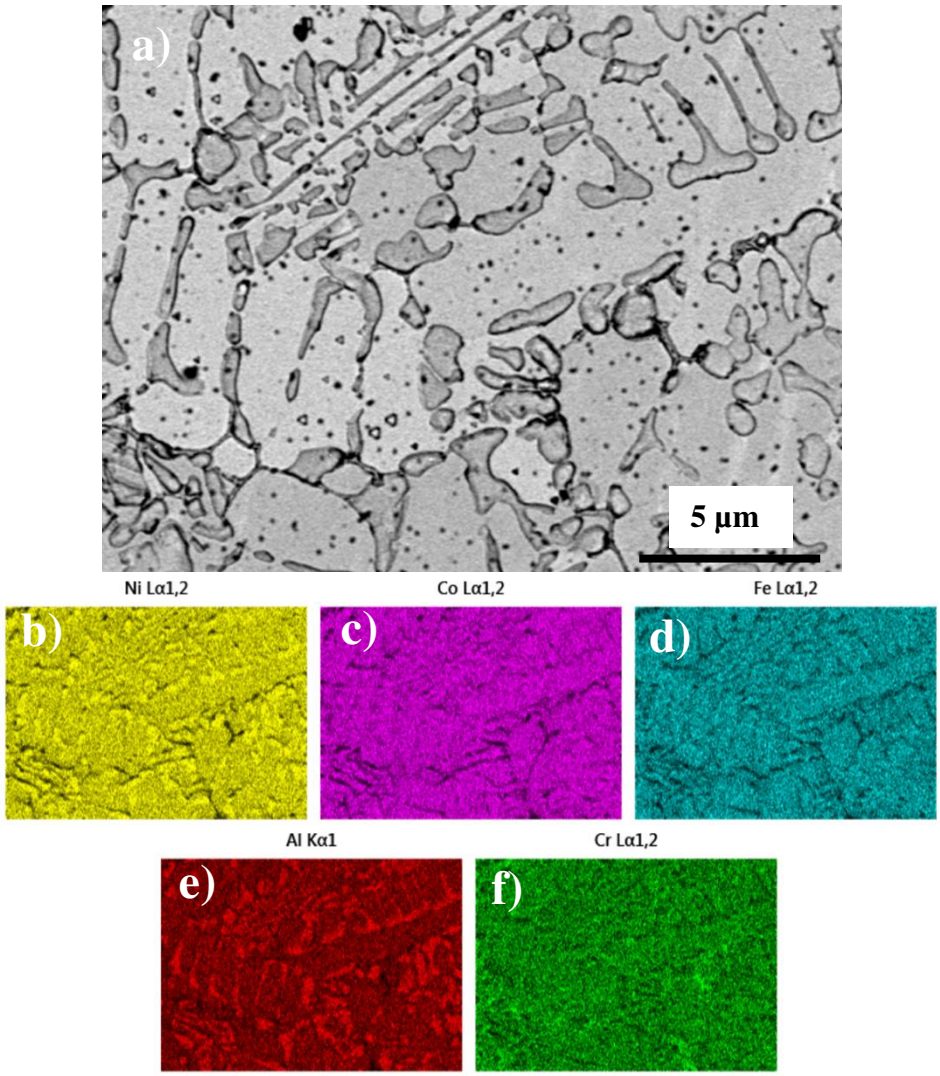

Figure 14: Al and Ni depleted (FCC) dendrite observed within a particle from the smallest powder-size fraction (38 µm < d < 53µm).

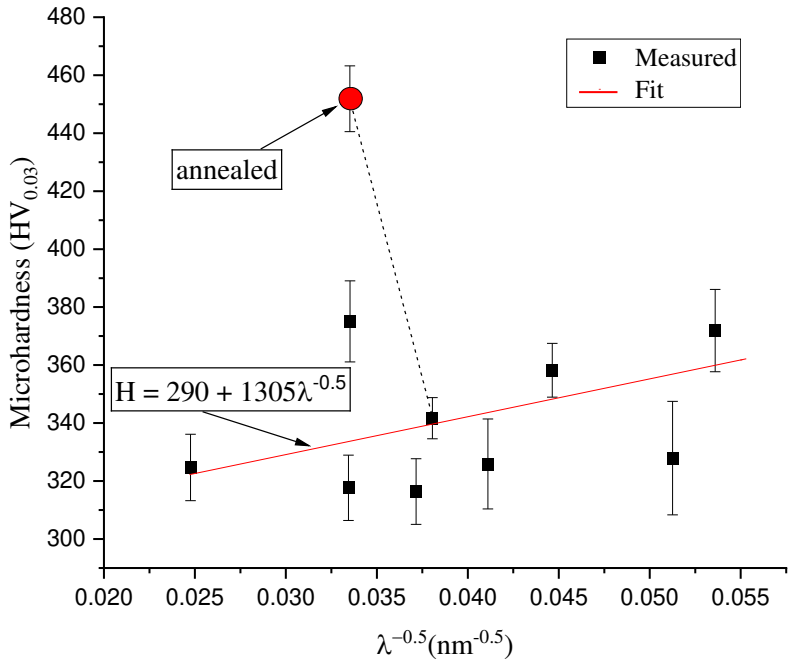

Figure 15: Microhardness of $AlCoCrFeNi_{2.1}$ powders as a function of lamellar spacing in a Hall-Petch plot.

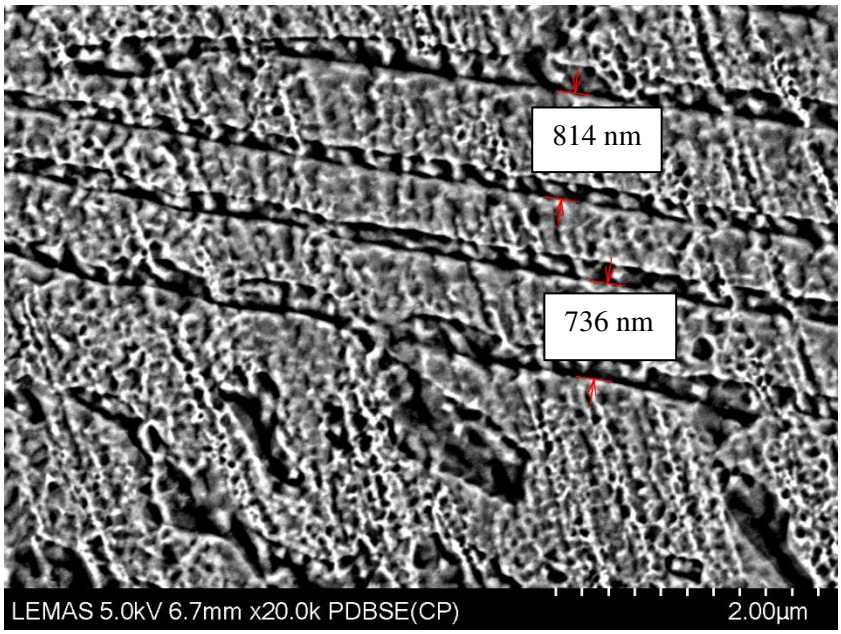

Figure 16: Backscattered SEM image of annealed particle from 150 - 212 µm size-fraction.

4. Summary

In this study powders were made from the $AlCoCrFeNi_{2.1}$ high-entropy alloy using a drop-tube facility. The sizes of the retrieved powders ranged from > 850 µm to 38 µm, with a corresponding range of cooling rates from 114 K s^{-1} to 1.75×10^6 K s^{-1}. Based on the results and discussion presented above the following conclusions can be drawn:

1. Faster cooling rates in $AlCoCrFeNi_{2.1}$ powders favour the formation of the FCC phase over the BCC and favour dendritic growth, leading to dendritic microstructures with a eutectic in the interdendritic regions.
2. BCC dendrites are observed in where $d < 212$ µm, although FCC dendrites remain the dominant primary solidification microstructure, suggesting that they are the fastest growing primary. The growth of BCC dendrites is attributed to a critical undercooling at which disorder trapping occurs, causing the growth velocity of the BCC phase to compete with the FCC phase. As long as the critical undercooling is not attained and B2 ordering is retained, the FCC phase retains the advantage of higher growth velocity.
3. Disorder trapping of the $L1_2$ structure is observed at 650 K s^{-1}, whereas the B2 ordered structure requires higher cooling rates to undergo the B2 – A2 transformation. In this work, disorder trapping of the B2 structure is achieved at 1.75×10^6 K s^{-1}. It may be possible that this can be achieved at lower cooling rates, although further TEM analysis would be required to reveal a closer estimate of the cooling rate required for the B2 – A2 transformation.
4. The microhardness of the powders shows a weak Hall-Petch relation, where the values of microhardness do not vary greatly from an average value of around 340 $Hv_{0.03}$. This is explained by the increasing FCC volume fraction with increasing cooling rate. Disorder trapping is also suggested to soften the microstructure and counter the strengthening effect of grain refinement.
5. As far as the microstructure morphology of the powders is concerned, it can be concluded that the microstructure evolves from regular/irregular eutectic to cellular/colony eutectic, followed by a dendritic structure with regular eutectic in the interdendritic region. Finally, at the highest cooling rate, a predominantly dendritic structure is observed with no eutectic observed in the interdendritic region.

5. References

[1] A. V. Kuznetsov, D.G. Shaysultanov, N.D. Stepanov, G.A. Salishchev, O.N. Senkov, Tensile properties of an AlCrCuNiFeCo high-entropy alloy in as-cast and wrought conditions, Mater. Sci. Eng. A. 533 (2012) 107–118. https://doi.org/10.1016/j.msea.2011.11.045.

[2] Y.J. Zhao, J.W. Qiao, S.G. Ma, M.C. Gao, H.J. Yang, M.W. Chen, Y. Zhang, A hexagonal close-packed high-entropy alloy: The effect of entropy, Mater. Des. 96 (2016) 10–15. https://doi.org/10.1016/j.matdes.2016.01.149.

[3] F. Otto, Y. Yang, H. Bei, E.P. George, Relative effects of enthalpy and entropy on the phase stability of equiatomic high-entropy alloys, Acta Mater. 61 (2013) 2628–2638. https://doi.org/10.1016/j.actamat.2013.01.042.

[4] Y.F. Kao, S.K. Chen, T.J. Chen, P.C. Chu, J.W. Yeh, S.J. Lin, Electrical, magnetic, and Hall properties of AlxCoCrFeNi high-entropy alloys, J. Alloys Compd. 509 (2011) 1607–1614. https://doi.org/10.1016/j.jallcom.2010.10.210.

[5] I.S. Wani, T. Bhattacharjee, S. Sheikh, Y.P. Lud, S. Chatterjee, P.P. Bhattacharjeea, S. Guo, N. Tsujib, Ultrafine-grained AlCoCrFeNi2.1 eutectic high-entropy alloy, Mater. Res. Lett. 4 (2016) 174–179. https://doi.org/10.1080/21663831.2016.1160451.

[6] S. Samal, M.R. Rahul, R.S. Kottada, G. Phanikumar, Hot deformation behaviour and processing map of Co-Cu-Fe-Ni-Ti eutectic high entropy alloy, Mater. Sci. Eng. A. 664 (2016) 227–235. https://doi.org/10.1016/j.msea.2016.04.006.

[7] L. Rogal, J. Morgiel, Z. Światek, F. Czerwiński, Microstructure and mechanical properties of the new Nb25Sc25Ti25Zr25 eutectic high entropy alloy, Mater. Sci. Eng. A. 651 (2016) 590–597. https://doi.org/10.1016/j.msea.2015.10.071.

[8] I.S. Wani, T. Bhattacharjee, S. Sheikh, P.P. Bhattacharjee, S. Guo, N. Tsuji, Tailoring nanostructures and mechanical properties of AlCoCrFeNi2.1 eutectic high entropy alloy using thermo-mechanical processing, Mater. Sci. Eng. A. 675 (2016) 99–109. https://doi.org/10.1016/j.msea.2016.08.048.

[9] Y. Lu, Y. Dong, S. Guo, L. Jiang, H. Kang, T. Wang, B. Wen, Z. Wang, J. Jie, Z. Cao, H. Ruan, T. Li, A promising new class of high-temperature alloys: Eutectic high-entropy alloys, Sci. Rep. 4 (2014). https://doi.org/10.1038/srep06200.

[10] P. Ding, A. Mao, X. Zhang, X. Jin, B. Wang, M. Liu, X. Gu, Preparation, characterization and properties of multicomponent AlCoCrFeNi2.1 powder by gas atomization method, J. Alloys Compd. 721 (2017) 609–614. https://doi.org/10.1016/j.jallcom.2017.06.020.

[11] T. Nagase, M. Takemura, M. Matsumuro, Microstructure of rapidly solidified melt-spun ribbon in AlCoCrFeNi2.1 eutectic high-entropy alloys, in: Mater. Sci. Forum, 2017: pp. 1350–1354. https://doi.org/10.4028/www.scientific.net/MSF.879.1350.

[12] A.M. Mullis, L. Farrell, R.F. Cochrane, N.J. Adkins, Estimation of cooling rates during close-coupled gas atomization using secondary dendrite arm spacing measurement, Metall. Mater. Trans. B Process Metall. Mater. Process. Sci. 44 (2013) 992–999. https://doi.org/10.1007/s11663-013-9856-2.

[13] Y.J. Liu, Z. Liu, Y. Jiang, G.W. Wang, Y. Yang, L.C. Zhang, Gradient in microstructure and mechanical property of selective laser melted AlSi10Mg, J. Alloys Compd. (2018). https://doi.org/10.1016/j.jallcom.2017.11.020.

[14] A.E. Nassar, A.M. Mullis, Rapid screening of high-entropy alloys using neural networks and constituent elements, Comput. Mater. Sci. 199 (2021) 110755. https://doi.org/10.1016/j.commatsci.2021.110755.

[15] F. He, Z. Wang, P. Cheng, Q. Wang, J. Li, Y. Dang, J. Wang, C.T. Liu, Designing eutectic high entropy alloys of CoCrFeNiNbx, J. Alloys Compd. 656 (2016) 284–289. https://doi.org/10.1016/j.jallcom.2015.09.153.

[16] M.R. Rahul, G. Phanikumar, Design of a Seven-Component Eutectic High-Entropy Alloy, Metall. Mater. Trans. A Phys. Metall. Mater. Sci. 50 (2019) 2594–2598. https://doi.org/10.1007/s11661-019-05210-3.

[17] H. Jiang, K. Han, X. Gao, Y. Lu, Z. Cao, M.C. Gao, J.A. Hawk, T. Li, A new strategy to design eutectic high-entropy alloys using simple mixture method, Mater. Des. 142 (2018) 101–105. https://doi.org/10.1016/j.matdes.2018.01.025.

[18] H.E. Cline, J.L. Walter, The effect of alloy additions on the rod-plate transition in the eutectic NiAl-Cr, Metall. Trans. 1 (1970) 2907–2917. https://doi.org/10.1007/BF03037830.

[19] D.R. Johnson, X.F. Chen, B.F. Oliver, R.D. Noebe, J.D. Whittenberger, Processing and mechanical properties of in-situ composites from the NiAlCr and the NiAl(Cr,Mo) eutectic systems, Intermetallics. 3 (1995) 99–113. https://doi.org/10.1016/0966-9795(95)92674-O.

[20] Y. Lu, X. Gao, L. Jiang, Z. Chen, T. Wang, J. Jie, H. Kang, Y. Zhang, S. Guo, H. Ruan, Y. Zhao, Z. Cao, T. Li, Directly cast bulk eutectic and near-eutectic high entropy alloys with balanced strength and ductility in a wide temperature range, Acta Mater. 124 (2017) 143–150.

https://doi.org/10.1016/j.actamat.2016.11.016.

[21] Y. Lu, H. Jiang, S. Guo, T. Wang, Z. Cao, T. Li, A new strategy to design eutectic high-entropy alloys using mixing enthalpy, Intermetallics. 91 (2017) 124–128. https://doi.org/10.1016/j.intermet.2017.09.001.

[22] D.B. Miracle, High-Entropy Alloys: A Current Evaluation of Founding Ideas and Core Effects and Exploring "Nonlinear Alloys," Jom. 69 (2017) 2130–2136. https://doi.org/10.1007/s11837-017-2527-z.

[23] D.L. Beke, G. Erdélyi, On the diffusion in high-entropy alloys, Mater. Lett. 164 (2016) 111–113. https://doi.org/10.1016/j.matlet.2015.09.028.

[24] T. Nagase, M. Takemura, M. Matsumuro, T. Maruyama, Solidification microstructure of AlCoCrFeNi2.1 eutectic high entropy alloy ingots, Mater. Trans. 59 (2018) 255–264. https://doi.org/10.2320/matertrans.F-M2017851.

[25] O. Oloyede, T.D. Bigg, R.F. Cochrane, A.M. Mullis, Microstructure evolution and mechanical properties of drop-tube processed, rapidly solidified grey cast iron, Mater. Sci. Eng. A. 654 (2016) 143–150. https://doi.org/10.1016/j.msea.2015.12.020.

[26] M.R. Abul, R.F. Cochrane, A.M. Mullis, Microstructural development and mechanical properties of drop tube atomized Al-2.85 wt% Fe, J. Mater. Sci. Technol. (2022). https://doi.org/10.1016/j.jmst.2021.05.085.

[27] F. Cardarelli, Materials Handbook — a concise desktop reference, Mater. Des. 22 (2001). https://doi.org/10.1016/s0261-3069(00)00075-3.

[28] J.H. Awbery, E. Griffiths, The latent heat of fusion of some metals, Proc. Phys. Soc. London. 38 (1925). https://doi.org/10.1088/1478-7814/38/1/343.

[29] E.S. Lee, S. Ahn, Solidification progress and heat transfer analysis of gas-atomized alloy droplets during spray forming, Acta Metall. Mater. 42 (1994) 3231–3243. https://doi.org/10.1016/0956-7151(94)90421-9.

[30] X. Gao, Y. Lu, B. Zhang, N. Liang, G. Wu, G. Sha, J. Liu, Y. Zhao, Microstructural origins of high strength and high ductility in an AlCoCrFeNi2.1 eutectic high-entropy alloy, Acta Mater. 141 (2017) 59–66. https://doi.org/10.1016/j.actamat.2017.07.041.

[31] L. Wang, C. Yao, J. Shen, Y. Zhang, T. Wang, Y. Ge, L. Gao, G. Zhang, Microstructures and room temperature tensile properties of as-cast and directionally solidified AlCoCrFeNi2.1 eutectic high-entropy alloy, Intermetallics. 118 (2020). https://doi.org/10.1016/j.intermet.2019.106681.

[32] M. Gao, D. Alman, Searching for Next Single-Phase High-Entropy Alloy Compositions, Entropy. 15 (2013) 4504–4519. https://doi.org/10.3390/e15104504.

[33] H. Zheng, R. Chen, G. Qin, X. Li, Y. Su, H. Ding, J. Guo, H. Fu, Phase separation of AlCoCrFeNi2.1 eutectic high-entropy alloy during directional solidification and their effect on tensile properties, Intermetallics. 113 (2019). https://doi.org/10.1016/j.intermet.2019.106569.

[34] N. Wang, B. Wei, Rapid solidification behaviour of Ag-Cu-Ge ternary eutectic alloy, Mater. Sci. Eng. A. (2001). https://doi.org/10.1016/S0921-5093(00)01954-7.

[35] C. Triveño Rios, M.F. Oliveira, R. Caram, W.J. Botta F, C. Bolfarini, C.S. Kiminami, Directional and rapid solidification of Al-Nb-Ni ternary eutectic alloy, Mater. Sci. Eng. A. (2004). https://doi.org/10.1016/j.msea.2003.10.187.

[36] C.R. Clopet, R.F. Cochrane, A.M. Mullis, The origin of anomalous eutectic structures in undercooled Ag-Cu alloy, Acta Mater. (2013). https://doi.org/10.1016/j.actamat.2013.08.001.

[37] R. Ahmad, R.F. Cochrane, A.M. Mullis, Disorder trapping during the solidification of βni 3Ge from its deeply undercooled melt, J. Mater. Sci. 47 (2012) 2411–2420. https://doi.org/10.1007/s10853-011-6062-y.

[38] Y.H. Meng, F.H. Duan, J. Pan, Y. Li, Phase stability of B2-ordered ZrTiHfCuNiFe high entropy alloy, Intermetallics. 111 (2019). https://doi.org/10.1016/j.intermet.2019.106515.

[39] A. Takeuchi, T. Wada, Y. Zhang, MnFeNiCuPt and MnFeNiCuCo high-entropy alloys designed based on L10 structure in Pettifor map for binary compounds, Intermetallics. 82 (2017) 107–115. https://doi.org/10.1016/j.intermet.2016.12.002.

[40] A.M. Mullis, O.E. Jegede, T.D. Bigg, R.F. Cochrane, Dynamics of core–shell particle formation in drop-tube processed metastable monotectic alloys, Acta Mater. 188 (2020) 591–598. https://doi.org/10.1016/j.actamat.2020.02.017.